Research Square

Preprints are preliminary reports that have not undergone peer review.
They should not be considered conclusive, used to inform clinical practice,
or referenced by the media as validated information.

Additive Manufacturing-Enabled EleCtroforming (AMEC) for Hot Isostatic Pressing Can Production

Vanshika Singh

singhv@ornl.gov

Oak Ridge National Laboratory

Amiee Jackson

Oak Ridge National Laboratory

Srikanth Allu

Oak Ridge National Laboratory

Rangasayee Kannan

Oak Ridge National Laboratory

Jason Mayeur

Oak Ridge National Laboratory

Tracy Yoho

A J Tuck (United States)

Dara Williams

A J Tuck (United States)

Fred List III

Oak Ridge National Laboratory

Sarah Graham

Oak Ridge National Laboratory

Leah Jacobs

Oak Ridge National Laboratory

Obaidullah Rahman

Oak Ridge National Laboratory

Julio Ortega Rojas

Oak Ridge National Laboratory

Amirkoushyar Ziabari

Oak Ridge National Laboratory

Peeyush Nandwana

Oak Ridge National Laboratory

M. Parans Paranthaman

Oak Ridge National Laboratory

Ryan Dehoff

Oak Ridge National Laboratory

Brian Post

Oak Ridge National Laboratory

Article

Keywords:

Posted Date: November 25th, 2026

DOI: https://doi.org/10.21203/rs.3.rs-11762633/v1

License: This work is licensed under a Creative Commons Attribution 4.0 International License.
Read Full License

Additional Declarations: Competing interest reported. The authors declare the following financial interests/personal relationships which may be considered as potential competing interests: UT Battelle LLC on behalf of Vanshika Singh, Brian Post, Srikanth Allu, Amiee Jackson, Rangasayee Kannan, Peeyush Nandwana, Parans Paranthaman, Dara Williams and Tracy Yoho has filed a jointly owned provisional patent application titled, ``ADDITIVE ELECTROFORMING HIP CANS FOR COMPLEX LARGE SCALE METALLIC STRUCTURES'' which is exclusively commercially licensed. If there are other authors, they declare that they have no known competing financial interests or personal relationships that could have appeared to influence the work reported in this paper.

Notice of Copyright: This manuscript has been authored by UT-Battelle, LLC under Contract No. DE-AC05-00OR22725 with the U.S. Department of Energy. The United States Government retains and the publisher, by accepting the article for publication, acknowledges that the United States Government retains a non-exclusive, paid-up, irrevocable, world-wide license to publish or reproduce the published form of this manuscript, or allow others to do so, for United States Government purposes. The Department of Energy will provide public access to these results of federally sponsored research in accordance with the DOE Public Access Plan (http://energy.gov/downloads/doe-public-access-plan).

Additive Manufacturing-Enabled EleCtroforming (AMEC) for Hot Isostatic Pressing Can Production

Vanshika Singh[1*], Amiee Jackson[1], Srikanth Allu[2], Rangasayee Kannan[1], Jason Mayeur[1], Tracy Yoho[3], Dara Williams[3], Fred List III[1], Sarah Graham[1], Leah Jacobs[1], Obaidullah Rahman[4], Julio Ortega Rojas[1], Amirkoushyar Ziabari[4], Peeyush Nandwana[5], M. Parans Paranthaman[6], Ryan Dehoff[1], Brian Post[1]

[1*]Manufacturing Science Division, Oak Ridge National Laboratory, 2350 Cherahala Blvd, Knoxville, 37932, TN, US.
[2]Computational Science and Engineering Division, Oak Ridge National Laboratory, 1 Bethel Valley Rd, Oak Ridge, 37830, TN, US.
[3]A.J. Tuck Co., 32 Tucks Rd, Brookfield, 06804, CT, US.
[4]Electrification and Energy Infrastructure Division, Oak Ridge National Laboratory, 1 Bethel Valley Rd, Oak Ridge, 37932, TN, US.
[5]Material Science and Technology Division, Oak Ridge National Laboratory, 1 Bethel Valley Rd, Oak Ridge, 37932, TN, US.
[6]Chemical Sciences Division, Oak Ridge National Laboratory, 1 Bethel Valley Rd, Oak Ridge, 37830, TN, US.

*Corresponding author(s). E-mail(s): singhv@ornl.gov;
Contributing authors: jacksonac@ornl.gov; allus@ornl.gov; kannanr1@ornl.gov; mayeurjr@ornl.gov; tyoho@ajtuckco.com; dwilliams@ajtuckco.com; listfaiii@ornl.gov; grahams@ornl.gov; jacobslj@ornl.gov; rahmano@ornl.gov; ortegarojajc@ornl.gov; ziabariak@ornl.gov; nandwanap@ornl.gov; paranthamanm@ornl.gov; dehoffrr@ornl.gov; postbk@ornl.gov;

Abstract

Powder Metallurgy-Hot Isostatic Pressing (PM-HIP) for near net shape production is an attractive manufacturing route that has the potential to strengthen

domestic energy resiliency and supply chain. However, complex-shaped HIP can production for PM-HIP is tedious and challenging. In this research we developed an alternative can production technology leveraging electroforming that combines precision and complexity. The process established is called "Additive Manufacturing-Enabled EleCtroforming (AMEC)" wherein on a polymer additively manufactured mandrel (the substrate), pure Ni will be electroformed to form a thick hollow shell like HIP can structures. Next, the can is filled with metal powder and HIP-ed to produce solid metallic part. For experimental purposes, a $\mathbf{6}^{"} \times \phi\ \mathbf{4}^{"}$ cylindrical and $\sim$2 mm thick leak-free electroformed nickel HIP can was manufactured. A near fully dense final part was achieved by HIPing SS316L powder infilled in this can. Distinct feature identification in the XCT reconstructed data of the hollow high aspect ratio the HIP can was enabled using Model Based Iterative Reconstruction (MBIR) and AI-enabled reconstruction algorithm that combines deep learning, physics-based modeling, and CAD data (Simurgh). Based on XCT and Bluelight scanning data, a wall thickness variation was observed in the electroformed Ni HIP can. However, based on experimental and computational model of HIP shrinkage, variation in wall thickness locally affected the rate of densification but overall didn't hinder the final densification of the can which remained uniform throughout the geometry. Finally, an AMEC-fabricated impeller was produced demonstrating high-fidelity complex shaped HIP can production in "One-Shot" with required dimensional accuracy, demonstrating the method's capability for complex PM-HIP components fabrication.

Keywords: Electroforming, Powder Metallurgy - Hot Isostatic Pressing (PM-HIP), Advanced Manufacturing, Near Net Shape

1 INTRODUCTION

Nuclear energy sector offers 20% of the overall U.S. electricity supply and 56.1% of the emission-free electricity becoming a crucial component of U.S. energy portfolio. With Nuclear Renaissance in U.S., lately, there has been growing thrust for small modular reactors (SMRs) and advanced reactors to fulfill the energy requirements. As opposed to onsite-production, factory-relied manufacturing for SMRs and Advanced reactors emerge as more economical and feasible to achieve nuclear infrastructure. The production of large pressure vessels for reactors like Generation III+ requires steel ingots as heavy as >600 tons; consequently, requiring the forging presses ranging from 12,000 – 17, 000 tons [1]. Given the limited domestic castings and forging industries capacity and capabilities, it has been lately harder to rely on these without compromising on the functionality of the design. With only five domestic large-forging facilities with maximum ingot size capability of 300 tons, it urges to look for alternative manufacturing processes [2]. Powder Metallurgy in combination with Hot Isostatic Pressing (PM-HIP) has emerged as a competent option to fulfill the production requirements. This process not only allows construction of complex alloys which otherwise is not possible but also offers lower or competitive cost than the forging+machining options without compromising on the mechanical properties such as tensile properties [1–3].

Amongst PM-HIP-ed demonstration of the complex components (valve bodies of 316L SS and grade 91 steel) included fabrication of reactor pressure vessel (RPV) upper head at 44% scale using low alloy A508 steel [4–7]. Electric Power Research Institute (EPRI) demonstrated fully densified RPV upper head assembly weighing 1650 kg and 50" diameter [1, 2]. However, the construction of the HIP can, which contains 27 integral penetrations, clearly demonstrate complex large can production as tedious and challenging. GE's study for fabricating a pipe-elbow shaped HIP can demonstrates the complicacy involved even for a moderately complex geometry [8]. Welding and joining of multiple subparts cause difficulty in creating leak-free can, adds time, and costs the can integrity. Currently, alternative methods for HIP can production uses advanced manufacturing techniques, such as wire arc additive manufacturing (WAAM) and powder based direct energy deposition process (DED) [9]. However, such processes inadvertently lead to high residual stresses and distortion and requires sophisticated toolpathing [10]. Large-scale additive manufacturing can achieve high complexity; yet it often sacrifices resolution. To adequately cater the manufacturing landscape for the energy sector, we need innovative techniques for complex, high resolution, scalable for HIP capsules.

We propose leveraging electroforming for HIP capsule production that combines precision and complexity. Electroforming is an electrochemical process of creating metallic components by depositing metal ions onto a negatively charged cathode [11, 12]. From the heavy manufacturing perspective, electroforming of Ni is widely deployed process in various sectors aerospace, oil & gas, and iron and steel industry for formation of thick corrosion-resistant coatings onto large complicated shaped parts such as valves and molds [11, 13, 14]. Apart from coatings, this has been leveraged to make shell like geometries such as heat shields and conformal cooling channels for rocket and aerospace applications [15–17]. One of its key characteristics is to provide high complexity and precision while also remains scalable at different length scales. In this work, we integrate electroforming process with fused filament fabrication approach (FFF) for mandrel production (sacrificial) to produce hollow leak-free HIP cans. In past decade, FFF has been extensively studied for small scale to large scale part production [18]. Additionally, large scale FFF namely Big Area Additive Manufacturing (BAAM) is one of the lowest energy intensity manufacturing processes (1.17 kWh/kg) [18] offering lesser residual stresses relative to metal based large scale AM process. The cost and time effectiveness of this process further allows faster iterative design change and advancements. Integrating FFF with electroforming allows scalability at different length scales and complexity concurrently.

Fig. 1 illustrates the detailed process flow that combines Electroforming process with polymer AM process. Initially mandrel is printed additively using FFF-based AM process and is conductively activated by silver spray application throughout the surface. The mandrel would be mounted as cathode into the electroforming bath. During the electroforming process, the metal that is required to be deposited (such as Ni, Cu) acts as anode, and the reaction between anode and cathode is enabled via electrolyte which is the same anode material-based salt. This induces flow of metal ions and enables its deposition onto the mandrel surface conforming to the shape of the mandrel. Further, the mandrel would be dissolved leaving the deposited metallic shell

which acts as the HIP can. Finally, the cans are filled with metal powder and HIP-ed (under high pressure and temperatures) to produce solid component. We define this process as "Additive Manufacturing Enabled EleCtroforming (AMEC)" process for HIP Can production. In this study, the concept was demonstrated and evaluated using a simple cylindrical geometry by fabricating a nominally 2 mm-thick Ni HIP can and densifying it with SS316L metal powder through the HIP process to assess feasibility. In addition, the study investigated unintended consequences of the electroforming process, such as non-uniform wall thickness, and their effect on the final densified metal part.

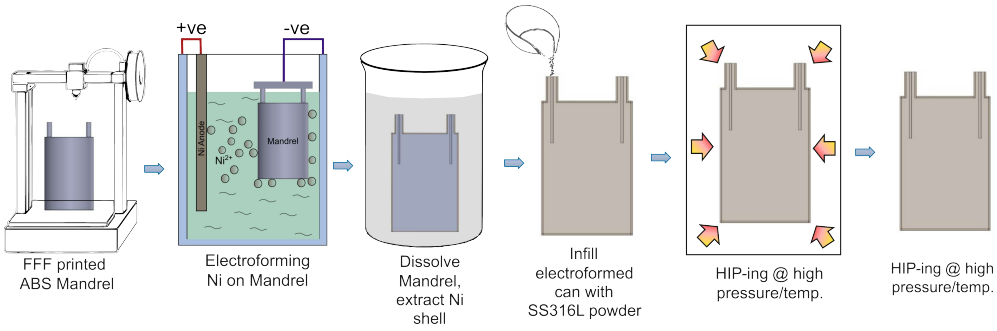

Fig. 1 Process flow for electroformed HIP can production for simple geometry (cylinder) and its HIPing

2 RESULTS

2.1 THE CHARACTER OF ELECTROFORMED NI

The Electron Backscatter Diffraction (EBSD) of the electroformed Ni (hollow can) exhibited fine, textured grains. Inverse Pole Figure (IPF) maps for two different cross-sections (front and top) is presented in Fig. 2a. In electroforming process, since the Ni ions are depositing onto the mandrel in the radial direction growing outwards; intuitively, the grain growth orientation aligns with the Ni deposition direction for both front and top cross-sections which is clear from the IPF maps. Fig. 2c presents the respective polar figures clearly indicating the strong texturing along <001>. The estimated grain size was found to be 21.03 μm for top cross-section and 28.46 μm for front cross-section respectively (Fig. 2d). Relative to additively manufactured pure Ni through laser powder bed fusion method [19] and laser DED process [20], electroformed Ni grains with standard industrial parameters led to finer grains. As per the hall-petch correlation which states that the flow stress is inversely proportional to the square root of the grain size qualitatively indicates that in electroformed deposited Ni, though textured, but finer grains would lead to higher strength at room temperature.

An important key trait for an ideal HIP can is the absence of any source of leak. Electroforming process onto FFF mandrel which originally doesn't have extremely

smooth surface compared to metal substrate could cause pore formation not only at the interface but potentially risk its propagation through thickness. Therefore, a porosity check is compulsory to identify any potential source of leakage or failure during the HIPing process. Optical micrograph (see Fig. 2b) indicated highly dense electroformed deposition through wall thickness except for the initial deposition region near the mandrel surface. Apparently, the initial pore formation near the polymer substrate did not propagate through thickness of Ni deposit. The density further calculated using Archimedes principle was 8.85 and 8.88 g/cc which is equivalent to 99.4% and 99.7% of the theoretical value. This increases the confidence in low potential for source of porosity-induced leak failure during the HIP cycle.

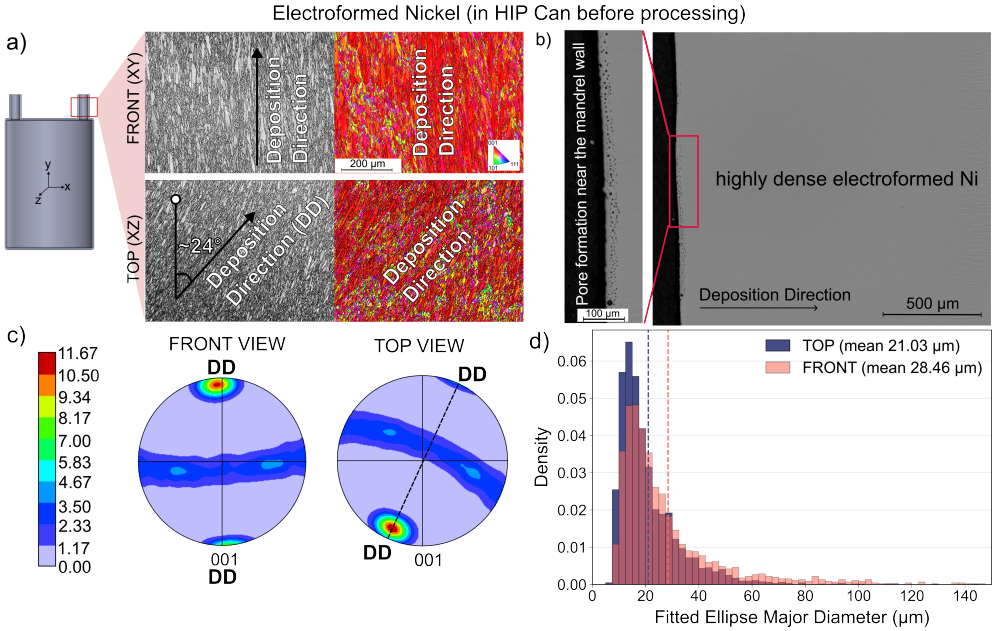

Fig. 2 a) EBSD Images of IPF Y maps respectively for electroformed Ni for both front and top view; b) Optical micrograph image for electroformed Ni for pore identification, if any; c) Polar plots for electroformed Ni deposits; d) Grain size distribution for electroformed Ni

2.2 DEPOSITED NI THICKNESS VARIATION

Electroforming that innately induces non-uniformity of the deposited thickness throughout the geometry required to be studied and understand if the non-uniform walls do and/or how that affects final densification outcomes. The X-ray Computed Tomography (XCT) of the HIP can was conducted and analyzed to understand the wall thickness non-uniformity across the geometry and is presented in Fig. 3a and b. Due to high aspect ratio of Ni hollow can and associated challenges of beam hardening effect and noise makes it non-trivial to reconstruct the XCT raw data using

standard procedure. Using the stated methodology in Appendix A, 3D reconstructed XCT of the electroformed Ni HIP can and the corresponding top (XZ) and front (XY) cut section of the XCT can is illustrated in Fig. 3a. Thickness distributions were calculated separately for the sidewall, top lid, and bottom lid. For each region, the mean, standard deviation, and median were reported. Median-based statistics were emphasized because incomplete segmentation and beam-hardening-related gaps can introduce outliers, particularly in the lid regions. Leveraging the external profile of the electroformed Ni Can constructed using bluelight scanning procedure using GOM scanner, the accurate thickness at the side, top and bottom of the can was estimated for the uniformly distributed discrete points. The XCT-derived thickness distributions agreed well with the GOM-based reference measurements for the sidewall and top lid, whereas a larger discrepancy was observed for the bottom lid (see Fig. 3b). Although both lids were reconstructed under the same challenging long-path X-ray geometry and were therefore similarly affected by scatter and beam-hardening artifacts, the bottom lid was slightly thicker. Unlike traditional XCT reconstruction methodology, the advanced reconstruction algorithms substantially mitigated scatter-related artifacts in both lid regions, residual scatter remained and reduced boundary contrast, making the segmentation more sensitive to reconstruction artifacts. Consequently, the bottom-lid thickness showed a larger discrepancy relative to the GOM reference, whereas the thinner top lid was recovered more accurately.

The data exhibited under deposition on the top lid followed by bottom lid and the sidewalls. The sidewalls maintained a nominal thickness of approximately 2.3 mm and 2.45 mm as per the GOM and XCT respectively as shown in Fig. 3b. Fig. 3a visually shows minimal variance in the side wall thickness circumferentially (in XY plane) as well as longitudinally (in the XZ plane). Contrastingly, the top lid had severe under deposition where locally the wall thickness went $\sim$0.35 mm near the port regions while $\sim$0.6 mm at the center of the top section per the GOM scanner calculations. XCT explicitly demonstrated similar behaviour showing the center of the top lid to be starkly thinner than the rest of the cylinder. At the bottom lid, corners of the can had over deposition causing the local thickness to rise up to 5 mm as per GOM. The over deposition might likely be attributed to the shorter current path length and the resulting locally elevated current density. Overall, bottom lid was thinner compared to side walls as per the GOM calculation and visually through XCT as well for the slice shown in the Fig. 3a. The local wall thickness variation further entails studying its effect, if any, on the densification of the powdered metal in the can.

2.3 DENSIFIED HIP'ED PART AND ITS CHARACTERISTICS

Fig. 4a and b shows the HIPed can before and after HIPing of the electroformed can. Fig. 4c demonstrates the GOM comparison of the cans before and after HIPing showing approximately 35% volume shrinkage. The volume shrinkage occurred as expected due to inherent packing efficiency associated with spherical powders and is consistent with the reported shrinkage values for the HIP cans manufactured through conventional process. Study by Nag et al. [21] showed that using direct energy deposition (DED),

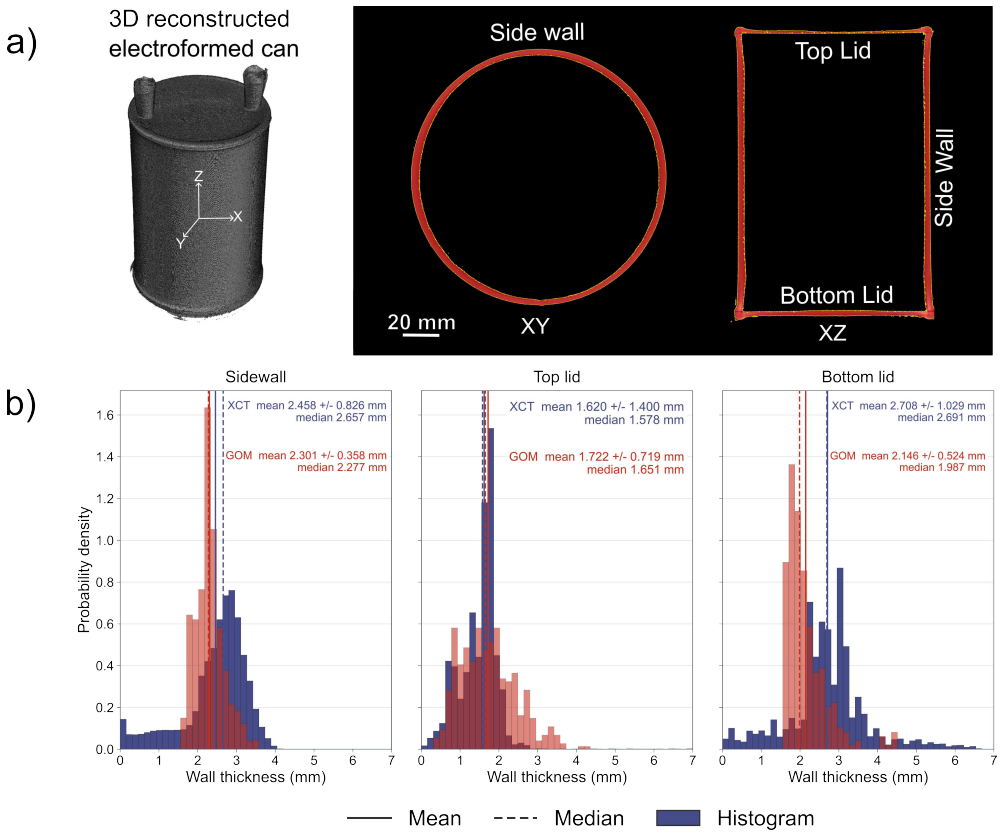

Fig. 3 a) 3D reconstructed XCT data of electroformed Ni can using the stated methodology in Appendix A and cross-section of the can in XY and XZ orientation; b) Wall thickness variation of the electroformed Ni can using XCT-based and GOM Scanner based approaches with mean and median marked for the side walls, the top lid of the can, and the bottom lid of the can

Laser Powder Bed Fusion (L-PBF), and conventional approach, the can shrunk by 32.1%, 31% and 34.3% respectively.

The measured GOM external volume of the pre-HIP can without Ni tubes is 1332.91 cc. The volume of the nickel in the can walls is 1300 g divided by 8.9 g/cc (mass/density) or 146.07 cc. Therefore, the internal volume, V_{int} of the can is 1186.84 cc. The density of the stainless steel powder is mass/volume or (7136-1300)/V_{int} = 4.92 g/cc. Since the density of 316 SS is 8.0 g/cc, the packing fraction for the 316 SS powder is 4.92/8.0 or 61.5%. The powder packing efficiency remained slightly below the theoretical packing efficiency for spherical particles; however, it was comparable to that achieved for the Praxair-procured powder and to results reported in similar studies employing alternative can manufacturing routes, indicating that appropriate powder filling practices were followed. The measured GOM external volume of the post-HIP can without tubes is 873.82 cc, and the volume of the nickel can is the same as before HIP (146.07 cc). So, the internal volume post HIP is 727.75 cc (874-146),

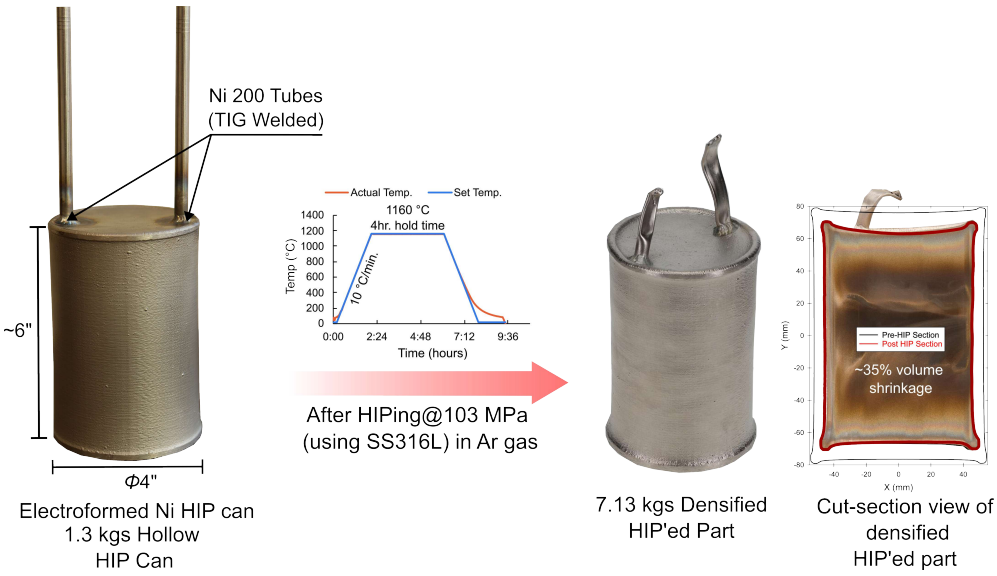

Fig. 4 a) HIPing of electroformed Ni can resulting in successful highly dense HIPed part. b) Blue light scanning of the can before and after HIPing demonstrated 35% volume shrinkage of the part.

and the mass of the powder is the same as before HIP (5836 g). The average density of the 316L within the can after HIP is 8.02 g/cc (mass/volume) or 100.2% of the theoretical value (8.0 g/cc). Calculations based on GOM indicates successful formation of a fully dense HIPed can.

Furthermore, combination of EBSD and EDS was used to study the fidelity of the HIPed densified part. Four regions namely 1 to 4 (see Fig. 5a) was chosen to encompass densified SS316L near nominal wall thickness (∼2 mm) as region-1, in the center of the part as region-2, under deposited wall (<1 mm) as region-3, and over deposited wall (>4 mm) as region-4. IPF X maps of each region and the corresponding Kernel Average Misorientation (KAM) maps are presented in Fig. 5b. IPF maps clearly demonstrates absence of any particular grain direction preference in either of the regions. In addition to visual appearances, the grain size distribution in either of the cases also remained in similar magnitude range of ∼10 μm as shown in Fig. 5c. Respective KAM maps for each case exhibited lower magnitudes of misorientation and remained largely <1°as observed from Fig. 5b and Fig. 5c. Lower KAM values and its identical behavior in each region reflects lower localized plastic deformation and lattice distortion. Overall for similar cylindrical geometry, different regions regardless of its position from the wall and/or wall thickness led to similar microstructural properties. A section of region 4 representing the transition from the coarser grained Ni can region to densified finer grained stainless steel region is shown in Fig. 5d. In addition to grain morphology uniformity observation within densified SS316L, the hardness of densified SS316L for each region was calculated and is listed in Table 1. The hardness of densified 316L remained in the similar range of ∼146-149 HV irrespective of the region, which is indicative of the minimal impact of wall thickness on mechanical properties.

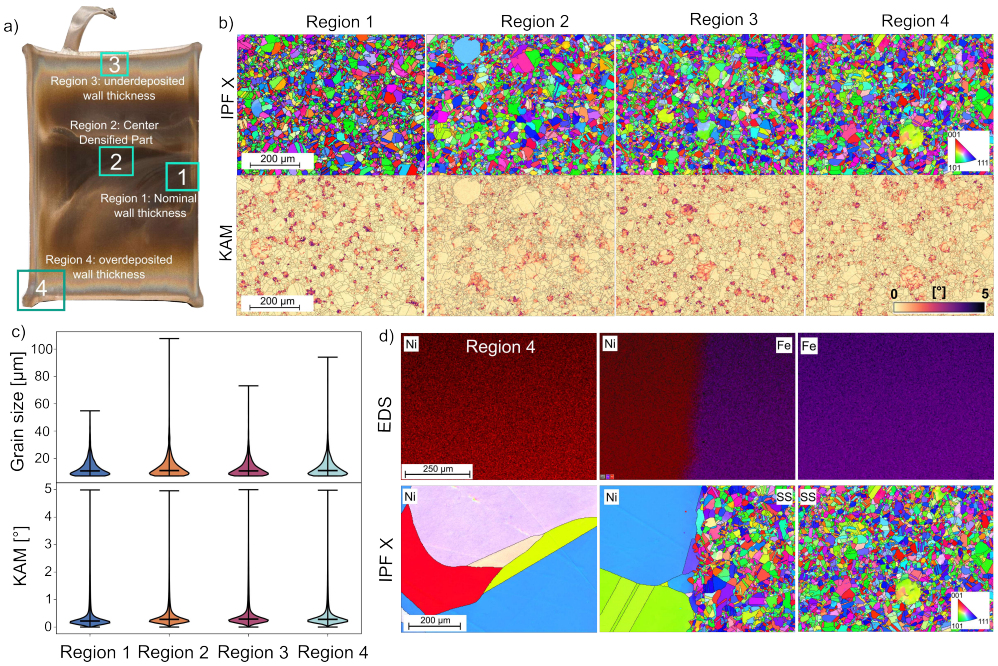

Fig. 5 a) Cross-section of the HIPed part showing different regions (1-4) selected for further investigation of microstructure and corresponding hardness properties; b) EBSD maps (IPF X) for regions 1 to 4 and the corresponding KAM maps; c) Grain size distribution and KAM distribution for each region; d) EDS and corresponding EBSD map (IPF X) for the Ni can, transition, and densified SS316L region for region 4

The EDS clearly showed distinct boundary from Ni can to stainless steel and exhibited minimal cross-diffusion of Ni and Fe in either of the sub-regions. Also, the IPF X demonstrated apparent transition from Ni to Stainless steel region. The Ni can region after densification showed extremely large grains in the order of 200 μm in contrast to initial electroformed Ni (before HIPing) grain size that was in the order of 20 μm, consistent with grain growth reported in pure Ni [22–24]. The substantial change in grain size of the electroformed Ni from room temperature before HIPing to the post-HIP condition is also evident in the approximately 50% drop in hardness (see Table 1).

2.4 COMPUTATIONAL MODELING OF DENSIFICATION AND DISTORTION

It is crucial to comprehend the shrinkage magnitude of the HIP can and densification characteristics of the powder; more specifically due to the non-uniform wall thickness variation that arises in case of electroformed Ni HIP can. Fig. 6a shows the overlay of experimental 2D profile of the electroformed HIP can and the simulated 2D profile after HIP shrinkage overall demonstrating a close match between both. The major variation was the bottom right corner of the HIP can where the simulated curve

Table 1 Hardness measurements (HV) of HIPed SS316L at different locations and Ni can (before and after HIPing)

Location	SS316L hardness	Ni hardness after HIP	Ni hardness before HIP
Region 1	146.07	81.38	—
Region 2	149.11	—	—
Region 3	149.21	77.73	—
Region 4	147.58	87.50	—
Front	—	—	159
Top	—	—	159

deviated ≈2 mm. The simulated densification of the SS316L powder is presented in Fig. 6b where four different regions are marked same as that shown in Fig. 5a except for region 4. Since cylinder is a symmetric feature, region 4 from fig. 6b and Fig. 5a are expected to display similar behavior. The HIP shrinkage model showed fully densified can in all regions with a slightly lower densification in region 4 but still a higher magnitude of ∼99%. The corresponding porosity maps of each region showed densification in the range of 99.71% to 99.95% (see Fig. 6b). The dissimilarity in the trend of densification magnitude for region 4 can be attributed to statistically smaller sample set for experimental porosity evaluation. The magnitude amongst all region varied 0.24% about the mean experimentally calculated porosity value and therefore it is assumed full densification in all regions equally regardless of the wall thickness variations. Even though the final state present the same densification, apparently the rate of densification differed amongst different regions. The relative density, which is change in density of the consolidating powder with time during the HIP process, and the pressure transmitted to the powder across the HIP can wall calculated through computational approach is shown is in Fig. 6c and d respectively. Region 1 which was closer to nominally thick wall (2.3 mm) had higher pressure transmission as opposed to the center of the can i.e., region 2; however, this didn't translate to differences in densification rate or final density. Contrastingly, the simulation shows that the region 4 exhibits the slowest rate of densification while region 3 has the steepest rate of densification. This can be clearly correlated to the pressure transmitted across a thin wall (region 3) where the wall thickness drops as low as 0.35 mm and a thick wall (region 4) where the wall thickness is up to 5 mm. Due to the stress shielding effect of the thick wall, there was lower pressure transmission with time leading to its slower densification and congruent argument can be made for region 3 with thin wall for higher rate of densification. Ajjarapu et al. [25] wherein they studied kinetics of densification with multiple SS316L HIP cans of different wall thicknesses also observed slower densification rates with thicker can walls with minimal impact on the final densification state.

3 DISCUSSION

The present results demonstrate the feasibility of combining polymer additive manufacturing with nickel electroforming to produce HIP cans capable of supporting SS316L

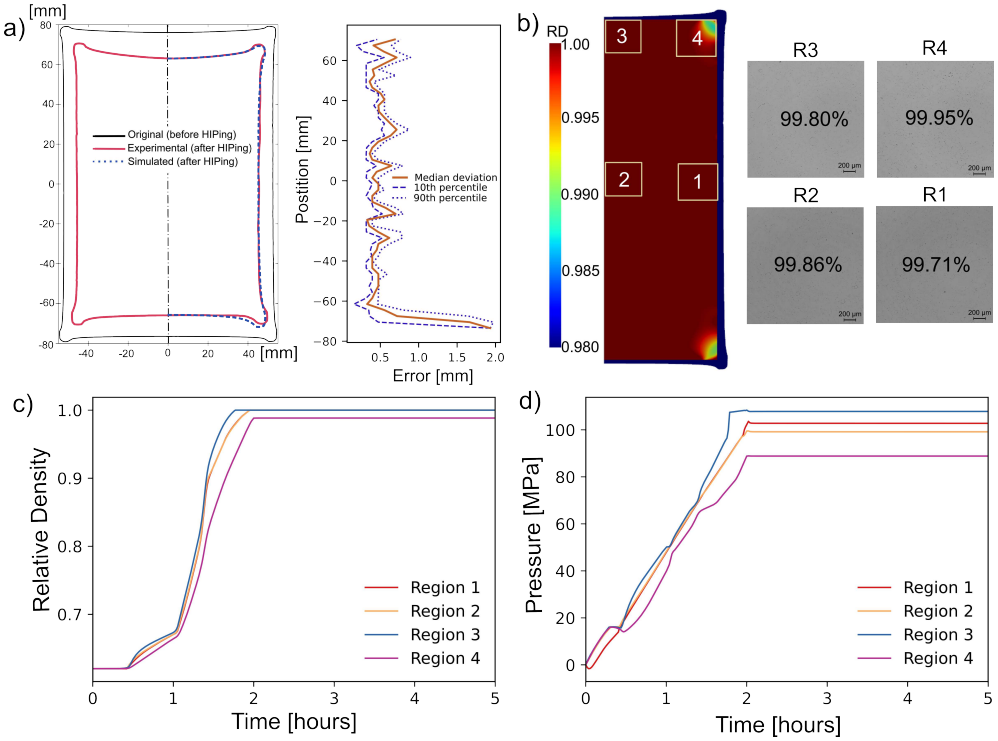

Fig. 6 a) Computed vs experimental shrinkage comparison, b) Computed relative density of the SS316L within the variable walled electroformed Ni HIP Can and porosity maps for corresponding regions from actual sample; c,d) Computed transient relative density and pressure transferred respectively

powder consolidation and producing a fully densified part. When extending AMEC to complex shaped geometries with intricate features, the wall thickness distribution could be more apparent and therefore poses as a potential challenge from the manufacturability stand point. A key additional observation was that the non-uniformity in the electroformed HIP can wall altered the densification rate locally due to the stress shielding effect. There is no pronounced effect on the final state of densification with non-uniform cylindrical HIP can wall thickness; however, it is currently unknown how would it translate to more complex shaped geometries. Therefore, it is critical to comprehend the fundamental mechanism inducing such variation.

The cylindrical sidewall was approximately 2.3 mm thick, the top lid was approximately 0.6 mm thick at its center and locally as thin as 0.35 mm near the ports, whereas deposition at the bottom corners reached approximately 5 mm. Thus, a nominal deposition thickness of 2 mm did not ensure a comparable minimum thickness throughout the can. Agreement between the GOM and XCT measurements supports the principal observation of top-lid under-deposition, although the greater discrepancy for the bottom lid warrants caution when interpreting its detailed thickness distribution.

The wall thickness variations can be understood through four coupled physical processes: electric-potential distribution, metal-ion transport, interfacial reduction kinetics, and additive-mediated surface growth. First, the arrangement of the anodes, cathode and fixtures, together with electrolyte conductivity and component geometry, determines the potential field and the distribution of current through the bath. Second, diffusion, electromigration and convection supply dissolved nickel species to the growing surface. Third, interfacial charge transfer converts these species into metallic nickel through the reaction $\mathrm{Ni}^{2+} + 2e^- \rightarrow \mathrm{Ni}$, at a rate governed by the local overpotential and surface concentrations. Fourth, additive adsorption and wetting modify the active surface, deposition kinetics and deposit morphology. These processes remain coupled as the deposited metal changes the surface geometry and, consequently, the surrounding electrical and concentration fields.

The connection between these processes and wall thickness follows Faraday's law:

$$h(\mathbf{x}, t) = \frac{M_{\mathrm{Ni}}}{2F\rho_{\mathrm{Ni}}} \int_0^t j_{\mathrm{Ni}}(\mathbf{x}, \tau)\, \mathrm{d}\tau, \tag{1}$$

where (h) is the local deposited thickness, (M_{Ni}) and (ρ_{Ni}) are the molar mass and density of nickel, (F) is Faraday's constant, and (j_{Ni}) is the positive magnitude of the local current density contributing to nickel deposition. The measured thickness therefore reflects the accumulated local nickel-deposition current rather than the bath-average applied current density alone. Variations in current efficiency, including losses to hydrogen evolution, can further modify this relationship. Consequently, increasing the total deposition time may thicken deficient regions while also increasing the existing excess at corners.

Corner over-deposition is consistent with current crowding at convex edges, where the electrolyte potential gradient can exceed that adjacent to flatter surfaces. Electrode spacing and orientation can reinforce this effect by providing lower-resistance current paths to particular regions. The comparatively thin top lid suggests a lower time-integrated nickel-deposition current over that surface. In the reported basket-anode arrangement, the sidewall may have had more favorable electrical access to the surrounding anodes than the lid center. Protruding ports and fixtures may also have redistributed current away from adjacent surfaces. These interpretations are consistent with the observed pattern, but assigning the variation solely to the shortest anode–cathode distance would overlook the three-dimensional potential field and interfacial polarization.

Spatial differences in mass transfer could amplify the electrical non-uniformity. Weak electrolyte renewal over the lid or around port bases would increase the local concentration-boundary-layer thickness and reduce the supply of nickel ions to the surface. Conversely, exposed edges may benefit from more effective replenishment. At high-current locations, however, rapid consumption can also produce stronger ion depletion and eventually constrain further growth. The reported bath circulation rate does not establish the local flow velocity or mass-transfer coefficient at these features. Accordingly, the thickness measurements alone cannot demonstrate that deposition was transport limited or identify mass transfer as the dominant cause of top-lid thinning. Local flow characterization and deposition measurements under controlled

changes in agitation would help distinguish insufficient ion supply from an unfavorable current distribution.

Surface chemistry provides another possible contribution. Additive coverage can vary with local transport and electrode potential, altering nickel deposition and leveling behavior. Wetting agents can facilitate bubble detachment, while persistent gas coverage can interrupt deposition and promote pits. Additives also influence internal stress and other deposit properties, so changes intended to improve thickness uniformity should be evaluated against can integrity. Uniformity of the initial conductive coating and the electrical contacts should also be controlled, particularly during establishment of a continuous nickel layer. None of these contributions was isolated in the present experiments; they therefore represent variables for targeted investigation rather than established explanations for the measured thickness pattern.

Practical improvements should address both excessive deposition and insufficient coverage. Electrically insulating shields positioned near the over-deposited corners could reduce local current crowding. Part orientation and electrolyte delivery offer complementary controls. Rotation about the cylinder axis could average circumferential differences in anode exposure, but would not necessarily correct a persistent difference between the lid and sidewall. Tilting or periodically reorienting the part could alter lid exposure, local flow and bubble release. The impeller demonstration illustrates the importance of these controls as geometric complexity increases. Fig. 7 shows the impeller HIP can produced via AMEC approach with a nominal intended thickness of 2 mm. XCT cross-section at different vertical heights shows a non-trivial high fidelity replication of the impeller mandrel profile. Its reproduced features establish the ability of AMEC to form intricate shells, while the observed over- and under-deposition show that geometric replication does not ensure uniform wall thickness. Blade edges, narrow passages and recessed surfaces introduce additional variations in electrical access and electrolyte renewal. A predictive design approach should couple the actual bath and fixture geometry with nickel-specific reaction kinetics, ion transport and surface growth, adding resolved fluid flow where transport effects are significant.

The effort to predict the electroformed HIP can thickness could then be two-way integrated with design for HIP shrinkage that informs the range of non-uniformity that could be afforded to achieve full-densification state and correspondingly fine tune the final electroforming parameters. On the other hand of mitigating the non-uniformity HIP can wall thickness due to its non-advantageous traits from manufacturability and final densification point of view, intentional non-uniform wall could be sporadically a desired feature as well. As noted by Huang et al. [26], uniformity in the wall thickness of pipe components produced by Near Net Shape (NNS) HIP could generate high cost penalty due to creep properties. Similarly, in case of turbine casing NNS HIP, suggested increasing wall thickness only at the creep limiting locations which could potentially offset the creep debit. Integrated prediction based approach and tailored AMEC could potentially layout a path forward for deliberate wall thickness control. While it is important tailoring and fundamentally controlling the non-uniformity generated during the AMEC process, it is vital emphasizing the fidelity of the shape of the can that could be achieved using AMEC as a “One-Shot” can production route

demonstrated via impeller HIP can production. Producing such complex shaped cans and concurrently avoid multiple sources of leakage via conventional routes of sheet metal operation is strenuously difficult. In addition to this, batch processing of multiple parts within same electrolytic bath also allows concurrent production of high mix (differently shaped and sized) low volume parts which are otherwise not trivial from both time and cost perspective via alternative routes.

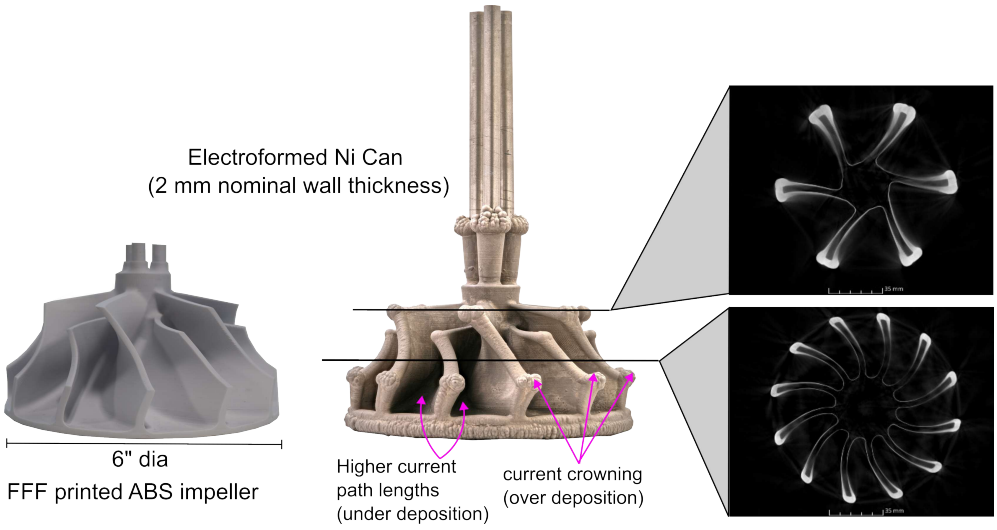

Fig. 7 FFF-printed ABS impeller shaped mandrel and the corresponding electroformed Hollow Impeller HIP can with nominal wall thickness of 2 mm. XCT cross-section at different vertical height of the can shows a non-trivial high fidelity replication of the impeller mandrel profile. Electroformed impeller can picture is highlighted with locations of over deposited and under deposited Ni regions requiring further fine tuning of electroforming process parameters

Outlook: The above methodology can be extrapolated to produce multi-material functional parts. Cu and Ni are well-studied materials that can be electroformed with high integrity on top of each other which can be further leveraged in combination with HIP-ing process to produce large scale multi-material parts. Fig. 8a shows the schematic of a prospective method of producing multi-material simple cylinder with sections of Cu-infilled material and the remainder of Ni-infilled material. Here we make two different mandrels. Initially, the first mandrel is electroformed with Cu, the polymer is dissolved and then the remaining cavity is infilled with Cu powder. The second polymer mandrel, which is the conjugate pair of the first mandrel, is joined with the Cu-infilled Cu can and then electroformed with Ni. The second polymer mandrel is dissolved and then the remaining cavity is infilled with Ni-based alloy powder. After intermediate pre-processing steps, the final can is HIP-ed and the multi-material component produced.

The design of the Cu mandrel, or Cu region, is not limited to the configuration shown in Fig. 8a. A wide range of Cu distributions, including lattice architectures

and other complex three-dimensional Cu networks embedded within Ni, could be produced using the electroforming-based approach (see Fig. 8b). This multi-material HIP can fabrication strategy could be applied to a variety of powder systems, including IN718/Cu, SS316L/Cu, H13/Cu, and tool steel/Cu combinations. In addition to the approach described above, the process can also be adapted such that all mandrels are electroformed in Ni and subsequently filled with dissimilar powder systems other than Cu, such as IN718/stainless steel, IN718/H13, and similar combinations. For different material systems, the HIPing parameters would require further evaluation. Nevertheless, the ability to fabricate multi-material HIP cans and the corresponding HIP-consolidated parts would enable the production of multifunctional components capable of meeting competing performance requirements, such as high strength and high thermal conductivity, which have recently emerged as critical objectives [27, 28].

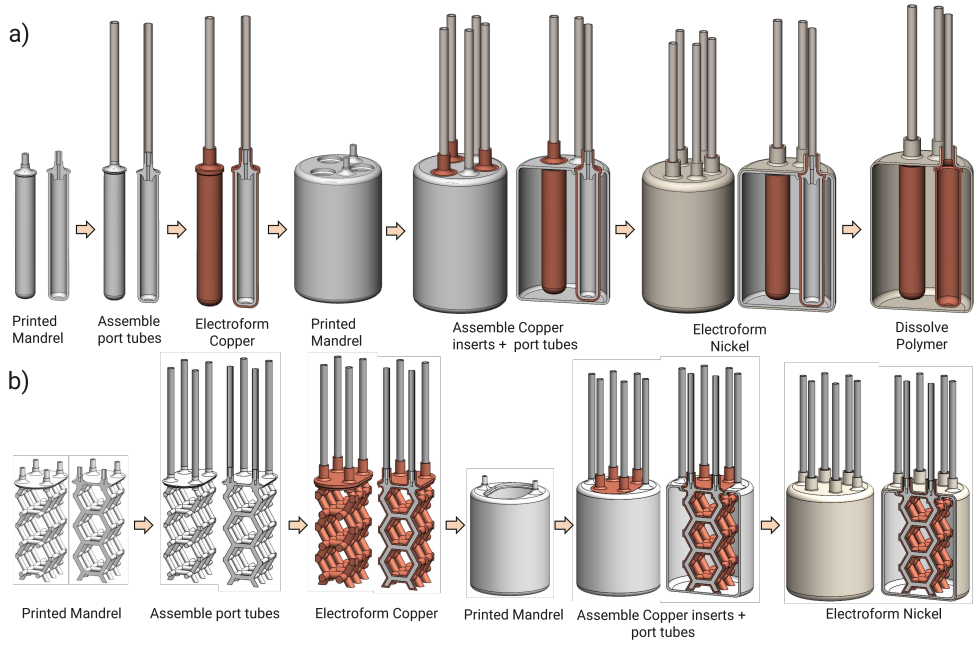

Fig. 8 Schematic of multi-material HIP can production process leveraging AMEC approach to produce to multifunctional metallic components. a) shows the process flow for simple configurations for multi-material AMEC approach while b) shows the extrapolation of the same component for further complex multi-material networks development utilizing this approach.

Conclusion: This research has developed AM electroforming process for HIP can production. This hybrid process, defined as "AMEC", integrated polymer additive manufacturing with electroforming process to develop leak free Nickel HIP cans. For experimental purposes a $6" \times \phi\ 4"$ cylindrical and ∼2 mm thick leak-free electroformed nickel HIP can was manufactured. Using the electroformed Ni can, a ∼100% fully-densified SS316L solid part was achieved. Combination of Artificial Intelligence

(AI) based XCT reconstructed and bluelight scanning thickness data of the electroformed nickel can showed a nominal wall thickness of ∼2.3 mm. However a variation in wall-thickness from 0.35 mm to 5 mm at edges and corners was observed. Through experimental and computational studies, minimal impact on the densification was observed with clear demonstration of nearly full densification in all regions showing porosity of more than 99.71% in all regions. Regardless of the wall thickness variation, the grain morphology and size variation of the densified SS316L remained in similar magnitude of ∼10 μm. Additionally, the Vicker's hardness values of the densified SS316L part minimally varied (146-149 HV) irrespective of the location.

Due to electroforming's innate ability to produce high precision and complex geometry replication, this research shows emergence of AMEC as promising alternative for "One-Shot" complex-shaped HIP can production. An impeller-shaped HIP can was fabricated with this process to highlight potential use for complex geometry. The AMEC-fabricated impeller can showed high fidelity conformal inner profile replication of the impeller shape which is non-trivial through conventional and alternative measures. However, due to the measured wall distribution of the cylinder and apparent observation of wall thickness variation in electroformed impeller, it makes it imperative to regulate the electroforming parameters using predictive modeling approach when successfully translating this to more complex geometries.

4 METHODS

Ni can manufacturing using electroforming: The mandrel design comprised a solid cylinder (150 mm tall, 100 mm outer diameter, 1 mm radius fillets on edges) with two ports (30 mm tall, 10 mm outer diameter, with a 3 mm diameter hole that extended 75.7 mm deep, 0.5 mm radius fillets on the top outer edges, and 1 mm radius fillets at the port base). These ports were equally spaced on an 80 mm diameter circle. The ports of the mandrels were designed such that the torque from installing threaded rods would be resisted. The mandrel was additively manufactured using Fused Filament Fabrication based approach through Xometry® using ABS-M30 on Stratasys 400/450 series with 0.010" layer height and 20% infill density. An appropriate surface finish is needed to avoid defects or sources for electroforming failure. Unevenness and protrusions on surfaces to be formed can induce delamination of the electroforming. For this, mandrel was vapor smoothed and de-burred to remove any large protrusions.

Prior to electroforming, the surfaces of FFF-printed polymer mandrel to be electroformed were made conductive by uniformly applying a silver coating. Once prepared, these mandrels were fixtured in the Ni electroforming baths. A schematic and the corresponding actual image of top view of Ni electroforming bath is presented in Fig. 9a. Anodes are pure Ni crowns procured from Nikkelverk and are spaced evenly across the length of the bath at 2 in., 26.5 in., and 49 in. as shown in Fig. 9a. All of the anode baskets are centered on their bars and encapsulated in green filter bags to avoid any contamination of the electrolyte bath. Cathode bars are centered between the anodes. The tank is equipped with two filter pumps, which are typically used to circulate the fluid to: i) enable flow of metal ions for electroforming process, ii) provide

continuous replenishment of electrolyte near the cathode regions, and iii) to minimize hydrogen bubble formation and thereby mitigate associated pitting defects. The flow rate maintain was 4500 liters/hour at 60 Hz. Table 2 shows the recommended range of electroforming process parameters in addition to the actual value used in this study. For Ni baths, temperature was set to 100.4 °F. An immersion heater with a feedback loop is typically used for temperature monitoring to minimize any temperature fluctuations introduced by open environment. pH is kept typically in the recommended range from the vendor and is measured using pH meter only once before the run and is not monitored throughout the run. Fig. 9b shows a schematic of a representative Ni electroforming bath with the additional chemicals for successful plating purposes. Boric acid is added as a buffer to limit the rise in pH at the cathode surface caused by hydrogen evolution, preventing incorporation of nickel hydroxide into the deposit; it has also been reported to suppress hydrogen evolution and improve current efficiency. Nickel hydroxide in the deposit makes the nickel brittle, stressed, and prone to pitting. Additives (Additive A/Snap L) percentage used in the setup is based on recommended values from the vendor in combination with heuristic approaches for fine tuning of the parameters. Surface tension values are measured using a tensiometer attached to a platinum wire which is dipped in the solution and pulled out, the bubble forms and breaks, reading the surface tension of the electrolyte. An average of 15 A/ft^2 was used as the current density for the electroforming operation. For 2 mm coating, the part remains in the bath for 112 hours. Once done, these cans were dipped into a bath of acetone to dissolve out the ABS-M30 material leaving an empty Ni can. A soap-leak test was conducted to evaluate leakage, if any.

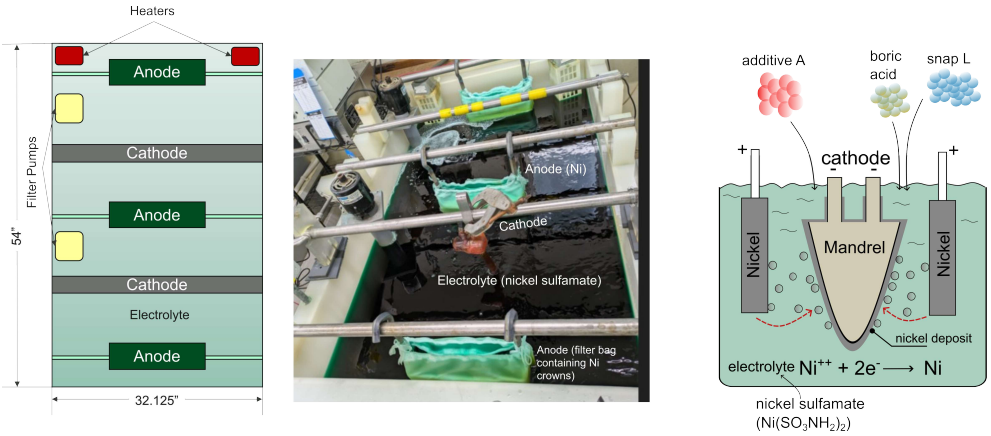

Fig. 9 a) Schematic (left) and actual electroforming setup (courtesy: AJ Tuck Co.) to electroform Ni onto mandrels (right). b) Schematic of electroforming process and shows that the electrolytic baths are added with additives, namely: Additive A, Snap L, and boric acid in this particular research.

Can preparation and HIPing parameters: The formed ports were cut off and pure Ni tubes were TIG welded with double weld passes in place. These Ni tubes facilitate powder infilling, degassing, and crimping purposes during preparation for HIP

Table 2 Electroformed Process Parameters

Process Parameters	Recommended Range	Used Value
Nickel (oz/gal)	9–12	9.37
Boric Acid (oz/gal)	4–6.5	4.8
Surface Tension (dynes/cm)	25–45	48
Additive A (oz/gal)	0.4–1.2	1.26
Snap L (%v/v)	0.1–0.4	0.16
Temperature (°F)	90–140	100.4
pH	3.8–4.2	4.1
Average Current Density (ASF)	–	15

cycle. Powder infilling, degassing, and sealing of the can was performed at American Isostatic Presses, Inc located in Columbus, Ohio. The furnace chosen was 9 inches in diameter and 27 inches tall to allow 6 inch tall cans (with ports, total height is 12 inch). Stainless steel 316L powder (typically used for Laser Powder Bed Fusion Process such as Concept Laser X1 line) from Praxair was chosen for an initial feasibility test. For HIPing, maximum peak temperature was set for 1160 °C for 4 hours with heating ramp rates at 10 °C/min. The isostatic pressure of 103.4 MPa (15,000 psi) was applied. The overall furnace operational time was 8 hours.

Geometric and Material Characterization: To study the wall thickness of the Ni can and measure it non-destructively, the electroformed hollow Ni HIP can was scanned with a VoluMax X-ray computed tomography (XCT) scanner for characterization and metrology. Peak X-ray tube voltage was 350 kV. A total of 2824 projections were measured in the angular range of [0°, 360°]. To reduce beam hardening artifacts, two source filters (Sn 2 mm, Cu 1.5 mm) were used. The reconstructed voxel size was 92 μm. To correct for beam hardening and scatter artifacts, 3D VSHARP® software (presented in [2]) was employed. A detailed post-processing of the XCT raw data for clear segmentation of the high-aspect ratio hollow can is described in Appendix A. Blue light 3D scanning was performed for the electroformed hollow Ni can before HIPing and for the densified part after HIPing using a GOM ATOS Q scanner with a resolution of about 30 μm. Zeiss Inspect metrology software was used to calculate the electroformed Ni wall thickness at uniformly distributed points using 3D CAD of the mandrel as the reference for the top lid, bottom lid, and side walls. Additionally, the software was also used to calculate dimensional changes and shrinkage of the can that accompanied HIPing. A thin 5 mm slice from the densified HIPed part was cut using wire electron discharge machining for further investigation. Two sets of metallographic samples were extracted from both the hollow can and densified part and polished to 0.05μm resolution using conventional sample preparation techniques for microstructure and mechanical property characterization. Bright-field optical imaging was performed using a Leica DMi8 inverted microscope to study volume fraction and distribution of porosity and defects within both pre- and post-HIPed parts. Scanning Electron Microscope (SEM) Energy Dispersive Spectroscopy (EDS) was conducted to study the elemental composition of the deposited Ni to ensure the purity of the deposited Ni. EDS was performed on a cross-section of the densified part, with particular focus on the steel-nickel interface, to correlate measured variations in mechanical

properties. Electron Beam Scatter Diffraction (EBSD) was conducted on pre- and post-HIPed parts to study the grain structure characteristics and its distribution. Both EBSD and EDS were performed using Zeiss Gemini 450 field emission scanning electron microscope (FE-SEM) using an Oxford UltimMax detector at an 8.6 mm working distance with 25 kV accelerating voltage. Vickers microhardness measurements were performed on both sets of metallographic samples to measure differences in both pre- and post-HIPed can and spatially within the densified part using a Leco AMH55 hardness tester.

Computational finite-element HIP shrinkage modeling details: Commercial FE software Abaqus/Standard was used to develop the 2D axisymmetric finite element (FE) model to simulate the SS316L powder densification and the electroformed HIP can shrinkage. For the geometry, a 2D profile extracted using GOM scanning of the electroformed Ni can and 2D cross-section from the CAD model of the mandrel was used to build the FE model (see Fig. B4). The bottom corner node was constrained in the y-direction; temperature and pressure ramp rates were applied in accordance with the experimental HIP cycle parameters. Both linear quadrilateral/CAX4T elements (84660) and linear triangular/CAXT elements (196) were used to construct the FE model leading to the total number of 85457 nodes and 84660 2D elements. The HIP can was modeled with classical rate-dependent J2 plasticity with temperature dependent properties. For the temperature-dependent thermo-physical properties of pure Ni, MPDB v10.09 (JAHM software) was utilized. While the SS316L powder was modeled as porous continuum using the Modified Cam-Clay Plasticity (MCCP) model and coupled its dependence on the relative density (i.e, the transient variation of the density of the powder during the consolidation process relative to full density) using user-defined fields in USDFLD subroutine. A detailed description of the parameterization of the SS316L powder consolidation constitutive model can be found in Mayeur et al. [29]. The temperature- and density-dependent constitutive properties for SS316L powder were determined from experimental data collected and reported in van Nguyen et al.[30] and Kohar et al.[31].

Acknowledgment. Research was performed at the U.S. Department of Energy's Manufacturing Demonstration Facility, located at Oak Ridge National Laboratory. This manuscript has been authored by UT-Battelle, LLC, under contract DE-AC05-00OR22725 with the US Department of Energy (DOE). The US government retains and the publisher, by accepting the article for publication, acknowledges that the US government retains a nonexclusive, paid-up, irrevocable, worldwide license to publish or reproduce the published form of this manuscript, or allow others to do so, for US government purposes. DOE will provide public access to these results of federally sponsored research in accordance with the DOE Public Access Plan (http://energy.gov/downloads/doe-public-access-plan).

This report was prepared as an account of work sponsored by an agency of the United States Government. Neither the United States Government nor any agency thereof, nor any of its employees, makes any warranty, express or implied, or assumes any legal liability or responsibility for the accuracy, completeness, or usefulness of any information, apparatus, product, or process disclosed, or represents that its use would not infringe privately owned rights. Reference herein to any specific commercial

product, process, or service by trade name, trademark, manufacturer, or otherwise does not necessarily constitute or imply its endorsement, recommendation, or favoring by the United States Government or any agency thereof. The views and opinions of authors expressed herein do not necessarily state or reflect those of the United States Government or any agency thereof.

Research sponsored by the U.S. Department of Energy, Office of Critical Minerals and Energy Innovation (CMEI), the Advanced Materials and Manufacturing Technologies Office through CRADA No. NFE-25-10906.

Thanks to Devin Slattery, Undergraduate Student at Worcester Polytechnic Institute for his part contribution towards CAD drawing for multi-material HIP can conceptualization during his internship at ORNL through U.S. DOE SULI Program.

Declarations

The authors declare the following financial interests/personal relationships which may be considered as potential competing interests: UT Battelle LLC on behalf of Vanshika Singh, Brian Post, Srikanth Allu, Amiee Jackson, Rangasayee Kannan, Peeyush Nandwana, Parans Paranthaman, Dara Williams and Tracy Yoho has filed a jointly owned provisional patent application titled, "ADDITIVE ELECTROFORMING HIP CANS FOR COMPLEX LARGE SCALE METALLIC STRUCTURES" which is exclusively commercially licensed. If there are other authors, they declare that they have no known competing financial interests or personal relationships that could have appeared to influence the work reported in this paper.

Appendix A X-ray computed tomography scan and reconstruction of the sample

To mitigate beam blockage, the canister was tilted prior to scanning (Figure A1). The scanner used was Zeiss' Volumax XCT system. The peak tube voltage was 350 kV and the current was 1.55 mA. The source-object and source-detector distances were 886.75 mm and 1327.94 mm, providing a magnification of 1.5X. 2824 projection measurements were taken over an angular range of 360° with an integration time of 500 ms. Each projection had 3024 × 3024 pixels with each pixel measuring 0.139 mm × 0.139 mm. The reconstruction voxel size was set to 92.82 µm.

Given the high-aspect-ratio hollow geometry of the cylindrical HIP canister, achieving a high-resolution 3D reconstructed volume is non-trivial due to the significant effects of noise, scatter, and beam hardening. We evaluated several reconstruction techniques sequentially to optimize reconstruction quality. The baseline method, Feldkamp-Davis-Kress (FDK [32]) – a standard algorithm for industrial cone-beam XCT—does not model underlying measurement noise. Consequently, FDK yielded substantial beam hardening and scatter artifacts, resulting in inconsistent intensities. This internal fogginess impeded wall segmentation, and the top and bottom lids failed to reconstruct accurately. Two correction techniques, LEAP [33] and 3DVsharp [34], were assessed. FDK combined with 3DVsharp outperformed LEAP, yielding more

prominent lids and sharper wall definition. The lids induce maximal X-ray beam attenuation, particularly when the beam traverses the lid plane. Because FDK weights all projections equally, it fails to account for measurement noise. We therefore employed a maximum likelihood (ML) method, an iterative technique that models photon noise and down-weights less reliable projections. This approach partially recovered the lids and further sharpened the walls. Finally, Simurgh [35] was applied to the ML reconstruction volume. Simurgh has shown to demonstrate efficacy under highly challenging XCT conditions by mitigating scatter, beam hardening, and noise while producing consistent textures. Simurgh successfully removed residual scatter and further resolved the lids.

Figure A2 displays a reconstruction slice through the wall (larger curve), the top lid (straight), and the port (smaller curve); two regions of interest (RoI, middle two rows), and an intensity profile plot along the straight line (bottom row). The RoIs demonstrates the progressive improvement in reconstruction quality from uncorrected FDK to 3DVsharp ML Simurgh. RoI 1 indicates that Simurgh reconstructs the lid with higher fidelity than the other techniques, while RoI 2 demonstrates that Simurgh yields the sharpest reconstruction. Uncorrected FDK exhibits severe beam hardening (elevated intensity on the outer wall, reduced intensity on the inner wall) and significant scatter (air voxel intensity inside the canister exceeds that of the exterior). The profile plots (along the line that intersects the wall and the top lid) further confirm that Simurgh successfully suppresses noise, beam hardening, and scatter artifacts.

Figure A3 shows the workflow involved in getting the final reconstruction volume. The artifacts in the measurement are corrected with 3DVsharp, followed by ML reconstruction which recovers some lost structures, and finally Simurgh that recovers more structure, removes artifacts and sharpens the image.

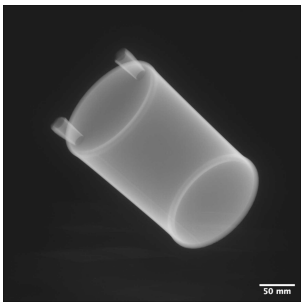

Fig. A1 A normalized projection measurement showing the tilted sample. Note that the XCT scan has a magnification of approximately 1.5X.

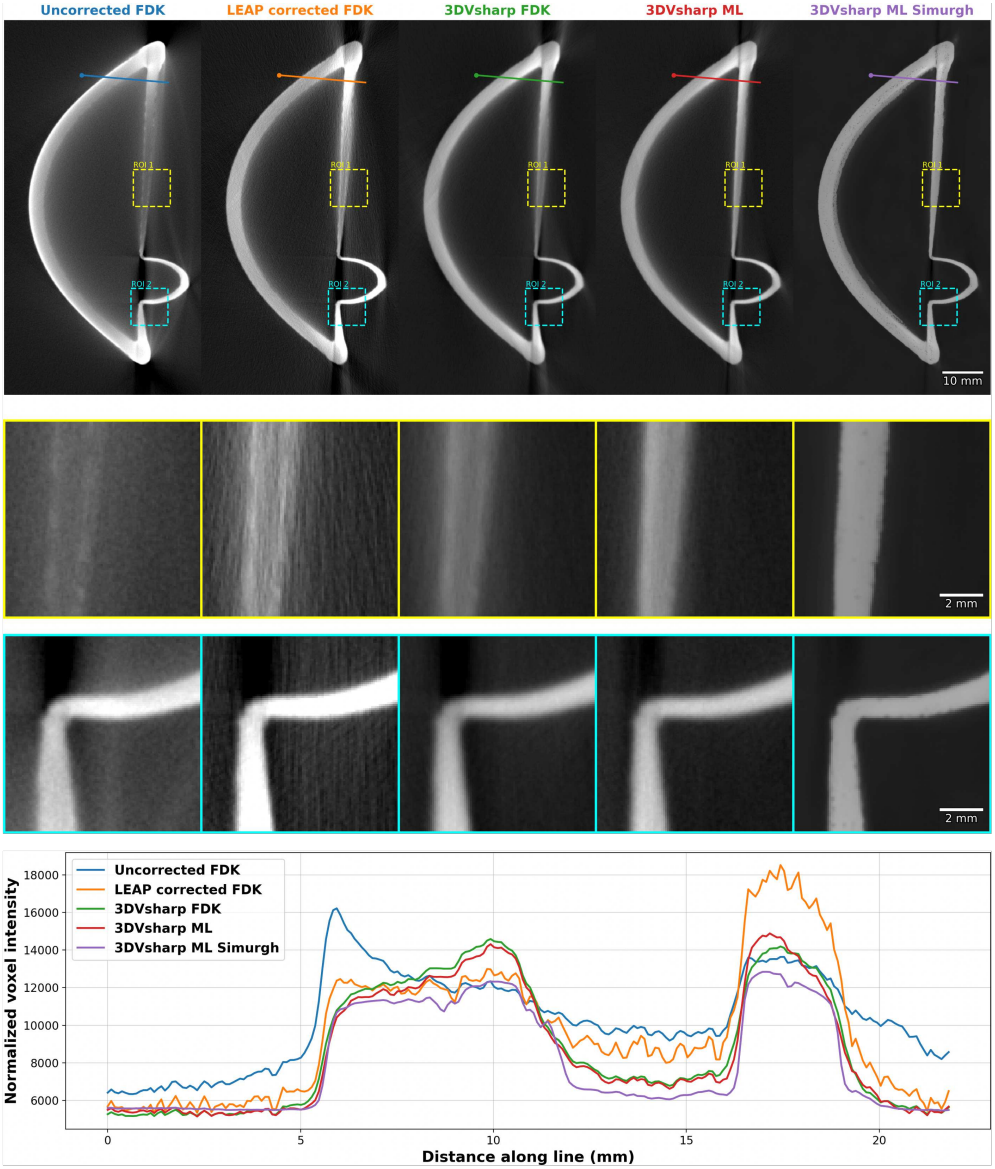

Fig. A2 (Top row): Left to right, An axial reconstruction slice from uncorrected FDK, LEAP corrected FDK, 3DVsharp FDK, 3DVsharp ML, and 3DVsharp ML Simurgh. (Middle two rows): The RoI from the top row showing a part of the top lid for each technique. (Bottom row): Profile plot, along a line that passes through the wall and the top lid, for each technique.

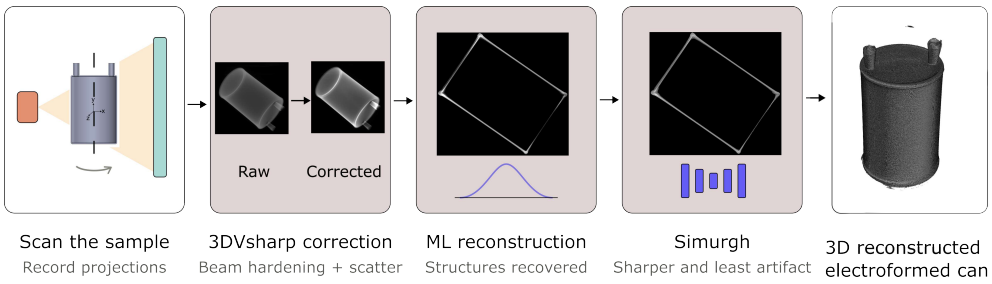

Fig. A3 X-ray CT workflow for artifact reduction: projection acquisition, 3DVsharp beam-hardening and scatter correction, maximum likelihood (ML) reconstruction, and Simurgh refinement.

Appendix B 2D FE Model for HIP shrinkage

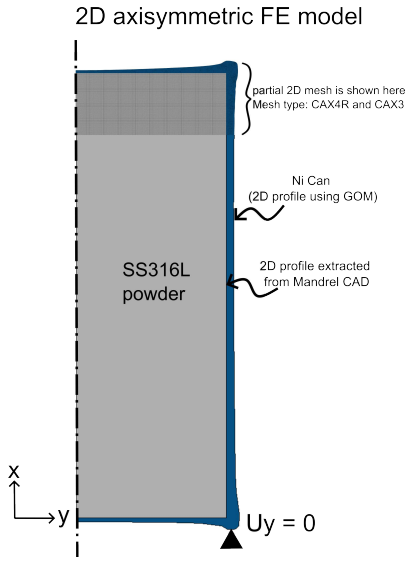

Fig. B4 2D FE Model Setup for HIP shrinkage - geometry and material details

References

[1] Gandy, D.: Small Modular Reactor Pressure Vessel Manufacturing & Fabrication Technology Development (2020)

[2] Hoelzer, D.T.: "The Use of Powder Metallurgy and Hot Isostatic Pressing for Fabricating Components of Nuclear Power Plants"

[3] Kinsey, S., Jessup, W., MPR Associates, Inc.: United States Nuclear Manufacturing Infrastructure Assessment. Technical Report DOE-MPRA–NE000638,

1494317 (December 2018). https://doi.org/10.2172/1494317 . http://www.osti.gov/servlets/purl/1494317/ Accessed 2025-02-21

[4] Gandy, D., Stover, C.: Advanced Manufacturing to Enable Next Generation of Nuclear Power Plants, Knoxville, TN, United States (2018). https://www.energy.gov/sites/prod/files/2019/02/f59/ne-amm-gandy-smr-rpv-manufacturing.pdf

[5] Gandy, D.: Innovative Manufacturing Process for Nuclear Power Plant Components via Powder Metallurgy & Hot Isostatic Pressing Methods (2016). https://www.energy.gov/sites/default/files/2015/12/f27/2%20-%20Innovative%20Manufacturing%20Process%20for%20Nuclear%20Power%20Plant%20Components.pdf

[6] Gandy, D.W.: PM-HIP for Nuclear: Outlook, Technology and Applications, pp. 1–10 (2023). https://doi.org/10.21741/9781644902837-1 . https://www.mrforum.com/product/9781644902837-1 Accessed 2026-09-21

[7] Horton, N., Sheppard, R.: Benefits of Tailoring Hot Isostatic Pressure/Powdered Metal (HIP/PM) and Additive Manufacturing (AM) to Fabricate Advanced Energy System Components, Pittsburg, PA (2015). https://www.netl.doe.gov/sites/default/files/event-proceedings/2016/crosscutting-ree/track-a-041916/Presentantion_20160419_0830A_FE0024014_EIO.pdf

[8] Huang, S.: Low Cost HIP Fabrication of Advanced Power Cycle Components and PM/Wrought Inconel 740H Weld Development. Technical Report DOE/NETL Award# DE-FE0031818, GE Research, Pittusburg, PA (September 2021). https://www.osti.gov/biblio/1822264

[9] Nag, S., Kameswara, P.K.A., List III, F., Mayeur, J., Meyer, L., Nycz, A., Dehoff, R.: Investigation of large-scale AM + PM parts for Nuclear Application. Technical report, Oak Ridge National Laboratory (ORNL), Oak Ridge, TN (United States), United States (2024). https://www.osti.gov/servlets/purl/2447309

[10] Solsbee, B.T.: Investigation of Finite Element Analysis Techniques for Direct Energy Deposition Additive Manufacturing. PhD thesis, The University of Tennessee, Knoxville, Knoxville, TN, United States (2024). https://trace.tennessee.edu/handle/20.500.14382/34290

[11] Parkinson, R.: Nickel Plating and Electroforming. In: Plating and Electroforming - Essential Industries for Today and The Future. The Nickel Development Institute, Toronto, Ontario (2001). https://nickelinstitute.org/en/resources/technical-guides/plating-and-electroforming-essential-industries-for-today-and-the-future-10088/

[12] Malone, G., Browning, M.E.: Electroforming. In: Cotell, C.M., Sprague, J.A., Smidt, F.A. (eds.) Surface Engineering, pp. 285–289. ASM International, Materials Park, OH (1994). https://doi.org/10.31399/asm.hb.v05.a0001263 .

https://dl.asminternational.org/handbooks/book/20/chapter/286046/Electroforming Accessed 2026-09-22

[13] Renner, T.: OPINION: The Power of Electroforming. Aviation Tech Today, United States (2023). https://www.aviationtoday.com/2023/07/14/opinion-the-power-of-electroforming/

[14] Parkinson, R.: Properties and applications of electroless nickel

[15] Kazaroff, J., Pavli, A.: Advanced tube-bundle rocket thrust chamber. In: 26th Joint Propulsion Conference. American Institute of Aeronautics and Astronautics, Orlando,FL,U.S.A. (1990). https://doi.org/10.2514/6.1990-2726 . https://arc.aiaa.org/doi/10.2514/6.1990-2726 Accessed 2026-09-29

[16] Malone, G.A., Winkelman, D.M.: High Performance Alloy Electroforming. Technical Report Bat Report No. 8874-927001, Bell Aerospace Textron Inc., Buffalo, New York (1989). https://ntrs.nasa.gov/api/citations/19890006670/downloads/19890006670.pdf

[17] Foreseer: How Perigee's Electroformed Combustor Improves Rocket Engines (2026). https://www.youtube.com/watch?v=mjsh242GJMc&t=3s

[18] Post, B.K., Lind, R.F., Lloyd, P.D., Kunc, V., Linhal, J.M., Love, L.J.: The Economics of Big Area Additive Manufacturing (2016)

[19] Li, C., Zhang, Q., Ren, Y., Chen, W., Li, W., Chen, J., Zhou, L.: Influence of energy density on the microstructure and property regulation of additive manufactured pure nickel. Advances in Mechanical Engineering **16**(2), 16878132241230228 (2024) https://doi.org/10.1177/16878132241230228 . Accessed 2026-10-15

[20] Zhang, W., Yin, Y., Feng, Y., Li, Q., Xu, D.: Formability, microstructure and properties of pure nickel fabricated via laser directed energy deposition. MW Metal Forming **6**, 87–92 (2025)

[21] Nag, S., Ajjarapu, P., Sarkar, S., List, F., Mayeur, J.: Convergent Manufacturing of Large- Scale Components for Nuclear Applications via Additive Manufacturing and Powder Metallurgy Hot Isostatic Pressing. Technical Report ORNL/TM-2025/4200, Oak Ridge National Laboratory (ORNL), Oak Ridge, TN (United States), Oak Ridge, United States (2025). https://www.osti.gov/servlets/purl/3002095

[22] Iordache, M.C., Whang, S.H., Jiao, Z., Wang, Z.M.: Grain growth kinetics in nanostructured nickel. Nanostructured Materials **11**(8), 1343–1349 (1999) https://doi.org/10.1016/S0965-9773(00)00427-X

[23] Wang, Y., Rohrer, G.S., Krause, A.R.: Twin formation during abnormal grain growth in pure Ni. Materialia **48**, 102782 (2026) https://doi.org/10.1016/j.mtla.

2026.102782

[24] Jin, Y., Lin, B., Bernacki, M., Rohrer, G.S., Rollett, A.D., Bozzolo, N.: Annealing twin development during recrystallization and grain growth in pure nickel. Materials Science and Engineering: A **597**, 295–303 (2014) https://doi.org/10.1016/j.msea.2014.01.018

[25] Ajjarapu, K., Dehoff, R.R., Nag, S.: Effect of Cannister Wall Thickness on Densification Pathways, Microstructure Evolution, and Mechanical Properties of Powder Metallurgy Hot Isostatically Pressed 316L Stainless Steel

[26] Huang, S.: Near-Net-Shape Hot Isostatic Press Manufacturing Modality for sCO2 CSP Capital Cost Reduction. DOE EERE Award#DE-EE0008996, GE Research, Niskayuna, NY (2023). https://www.osti.gov/biblio/2311108

[27] Gradl, P., Cervone, A., Colonna, P.: Integral Channel Nozzles and Heat Exchangers using Additive Manufacturing Directed Energy Deposition NASA HR-1 Alloy (2022)

[28] Marques, A., Guimarães, B., Cerqueira, M., Silva, F., Carvalho, O.: Multi-Material Inconel 718 Parts with Highly Conductive Copper Cooling Channels for Aerospace Applications. Advanced Engineering Materials **25**(6), 2201349 (2023) https://doi.org/10.1002/adem.202201349 . Accessed 2026-11-09

[29] Mayeur, J.R., Ajjarapu, K.P.K., List, F.A., Sarkar, S., Nag, S., Dehoff, R.R.: Computational modeling of powder metallurgy hot isostatic pressing. Journal of Manufacturing Processes **176**, 46–60 (2026) https://doi.org/10.1016/j.jmapro.2026.08.043 . Accessed 2026-11-03

[30] Nguyen, C.V.: Numerical Simulation of Hot Isostatic Pressing with Particular Consideration of Powder Density Distribution and Temperature Gradient. Werkstoffanwendungen im Maschinenbau, vol. 11. Shaker Verlag, Aachen (2016). PhD dissertation, RWTH Aachen University, 2015. RWTH publication number RWTH-2016-04663

[31] Kohar, C.P., Martin, Étienne., Connolly, D.S., Patil, S., Krutz, N., Wei, D., Inal, K.: A new and efficient thermo-elasto-viscoplastic numerical implementation for implicit finite element simulations of powder metals: An application to hot isostatic pressing. International Journal of Mechanical Sciences **155**, 222–234 (2019) https://doi.org/10.1016/j.ijmecsci.2019.01.046

[32] Feldkamp, L.A., Davis, L.C., Kress, J.W.: Practical cone-beam algorithm. J. Opt. Soc. Am. A **1**(6), 612–619 (1984)

[33] Champley, K., Kim, H.: LEAP: LivermorE AI Projector for Computed Tomography. GitHub. Publication Title: GitHub repository (2024). https://github.com/llnl/LEAP

[34] Holt, K., Savaliya, D., Shiroma, A., Hu, M., Nisius, D., Hoelzer, S., Sun, M., Vernekohl, D., Star-Lack, J.: Design and optimization of 3D VSHARP scatter correction for industrial CBCT using the linear Boltzmann transport equation. In: 7th International Conference on Image Formation in X-Ray Computed Tomography, vol. 12304, pp. 269–275. SPIE, Baltimore, MD (2022). https://doi.org/10.1117/12.2647154

[35] Ziabari, A., Venkatakrishnan, S., Dubey, A., Lisovich, A., Brackman, P.D., Frederick, C.L., Bhattad, P., Bingham, P.R., Plotkowski, A.J., Dehoff, R.R., Paquit, V.C.: SIMURGH: A framework for CAD-driven deep learning-based x-ray CT reconstruction. In: 2022 IEEE International Conference on Image Processing (ICIP), pp. 3863–3867. IEEE, Bordeaux, France (2022). https://doi.org/10.1109/ICIP46576.2022.9898017